A&A 556, A117 (2013)
DOI: 10.1051/0004-6361/201321855

Astronomy & Astrophysics

Measurement of the earthshine polarization in the *B, V, R,* and *I* bands as function of phase

A. Bazzon[1], H. M. Schmid[1], and D. Gisler[2]

[1] ETH Zurich, Institute of Astronomy, Wolfgang-Pauli-Str. 27, 8093 Zurich, Switzerland
e-mail: bazzon@astro.phys.ethz.ch
[2] Kiepenheuer Institut für Sonnenphysik, Schöneckstr. 6, 79104 Freiburg, Germany

Received 7 May 2013 / Accepted 4 June 2013

ABSTRACT

Context. Earth-like, extrasolar planets may soon become observable with upcoming high contrast polarimeters. Therefore, the characterization of the polarimetric properties of the planet Earth is important for interpreting expected observations and planning of future instruments.
Aims. Benchmark values for the polarization signal of integrated light from the planet Earth in broad band filters are derived from new polarimetric observations of the earthshine backscattered from the Moon's dark side.
Methods. The fractional polarization of the earthshine p_{es} is measured in the B, V, R, and I filters for Earth-phase angles α between 30° and 110° with a new, specially designed wide field polarimeter. In the observations, the light from the bright lunar crescent is blocked with focal plane masks. Because the entire Moon is imaged, the earthshine observations can be corrected for the stray light from the bright lunar crescent and twilight. The phase dependence of p_{es} is fitted by a function $p_{es} = q_{max} \sin^2 \alpha$. Depending on wavelength λ and the lunar surface albedo a, the polarization of the backscattered earthshine is significantly reduced. To determine the polarization of the planet Earth, we correct our earthshine measurements by a polarization efficiency function for the lunar surface $\epsilon(\lambda, a)$ derived from measurements of lunar samples from the literature.
Results. The polarization of the earthshine decreases toward longer wavelengths and is about a factor 1.3 lower for the higher albedo highlands. For mare regions the measured maximum polarization is about $q_{max,B} = 13\%$ for $\alpha = 90°$ (half moon) in the B band. The resulting fractional polarizations for the planet Earth derived from our earthshine measurements and corrected by $\epsilon(\lambda, a)$ are 24.6% for the B band, 19.1% for the V band, 13.5% for the R band, and 8.3% for the I band. Together with the literature values for the spectral reflectivity, we obtain a contrast C_p between the polarized flux of the planet Earth and the (total) flux of the Sun with an uncertainty of less than 20%, and we find that the best phase for detecting an Earth twin is around $\alpha = 65°$.
Conclusions. The obtained results provide a multiwavelength and multiphase set of benchmark values that are useful for assessing different instrument and observing strategies for the future high contrast polarimetry of extrasolar planetary systems. Polarimetric models of Earth-like planets are in qualitative agreement with our results, but there are also significant differences that might guide more detailed computations.

Key words. polarization – Earth – Moon – instrumentation: polarimeters – scattering

1. Introduction

This paper presents polarimetric observations of the earthshine on the Moon's dark side in order to characterize the integrated polarimetric properties of the planet Earth for future investigations of Earth-like extrasolar planets. With the rapid progress in observational techniques, the detection of reflected light from terrestrial or even Earth-like extrasolar planets may become possible in the near future with high-contrast imaging of very nearby ($d \lesssim 5$ pc) stars. Statistical studies based on the radial velocity survey of stellar reflex motions due to low mass planets (Mayor et al. 2011) and the planetary transit frequency of small planets by the KEPLER satellite (Howard et al. 2012) both indicate that terrestrial planets could be present with high probability around every nearby star. The detection of a periodic RV-signal in α Cen B by Dumusque et al. (2012), which was attributed to a planet with a mass of $\approx 1\ M_{Earth}$, demonstrates that the nearest stars are really excellent targets for the search for extrasolar planets.

The intensity contrast between a reflecting planet and the parent star is

$$C_I(\alpha, \lambda) = f(\alpha, \lambda)(R_p/d_p)^2, \quad (1)$$

where α is the phase angle, R_p the radius of the planet, d_p its separation to the star, and $f(\alpha, \lambda)$ the phase-dependent reflectivity. Thus the contrast is high for small separations d_p, and the prospect of direct detection is particularly favorable for close-in planets $d_p \lesssim 0.3$ AU around nearby stars for which such a small separation planet can still be spatially resolved. However, detecting a faint signal from a reflecting planet at an angular separation of about 0.1 arcsec from a bright star is challenging and requires an instrument with high spatial resolution and very high contrast capabilities based on coronagraphy and some kind of differential imaging. The upcoming planet finder instruments SPHERE (Beuzit et al. 2008) and GPI (Macintosh et al. 2012) will both provide improved performance for substantial progress in this direction. A particularly promising technique for this search for reflected light from planets around the nearest stars is differential polarimetric imaging, which is available with the SPHERE instrument. With sensitive polarimetry one can search for a polarized signal owing to the scattered and therefore polarized light from the planet within the halo of the unpolarized light from the star (e.g. Schmid et al. 2006). The measureable polarization contrast can be described in a similar way to the intensity contrast by

$$C_p(\alpha, \lambda) = p(\alpha, \lambda) f(\alpha, \lambda)(R_p/d_p)^2, \quad (2)$$

where $p(\alpha, \lambda)$ is the integrated fractional polarization. Therefore, the investigation of $p(\alpha, \lambda)$ and the polarization flux $p(\alpha, \lambda) \times f(\alpha, \lambda)$ of planet Earth is important for planning future observing projects on extrasolar planetary systems and interpreting observational data. Up to now only very limited data are available for the integrated polarization of the planet Earth.

The oldest and still best polarization phase curve of Earth comes from the observations of the earthshine by Dollfus (1957). He determined the earthshine polarization phase curve $p_{es}(\alpha)$ with visual observations (V band) for Earth phase angles from $\alpha = 22°$, about 1.5 days after new moon, to about $\alpha = 140°$, between half and full moon. For dark regions (maria) on the Moon Dollfus (1957) finds a steady increase in the fractional polarization of the earthshine from about $p_{es} \approx 2\%$ around $\alpha = 30°$, to a maximum polarization of about $p_{es} \approx 10\%$ for $\alpha \approx 100°$, and a decline for larger α's down to $p_{es} \approx 4\%$ at $\alpha \approx 140°$. Dollfus (1957) also finds a higher fractional polarization for the backscattered light for dark regions with surface albedo of about $a = 0.1$ than for bright regions with $a = 0.2$. In addition he notes a wavelength dependence in the fractional polarization of the earthshine with higher values at shorter wavelength. One should note that backscattering at the lunar surface introduces a depolarization of the earthshine. Thus, the fractional polarization of the light scattered by Earth is higher by a factor of about 2 to 3 than the measured value from the backscattered earthshine.

Space experiments did not provide much progress because full Earth polarimetry was to our knowledge not taken or at least not published. Earth observing satellites with polarimetric capabilities took usually measurements of only small fractions of the Earth surface from which it is difficult to determine the net polarization for the entire planet. A result from the POLDER satellite was reported by Wolstencroft & Breon (2005), who obtained fractional polarization values for $\alpha = 90°$ for three wavelengths and different cloud coverages. For a typical value for the average cloud coverage of 55%, they derive for the polarization of the planet Earth: p(443 nm) = 22.6%, p(670 nm) = 8.6%, p(865 nm) = 7.3%.

An interesting new result on the Earth polarization from earthshine measurements is the VLT spectro-polarimetry from Sterzik et al. (2012), which show narrow spectral features due to water, O_2, and O_3 absorptions in the Earth atmosphere and a rise of the fractional polarization toward the blue due to Rayleigh scattering.

Model calculations have been made for the fractional polarization of the reflected light from Earth-like planets (Stam 2008), as well as the polarization produced by reflecting clouds (e.g., Karalidi et al. 2011, 2012; Bailey 2007) or glint from ocean water surfaces (Williams & Gaidos 2008). The models provide an adequate description of the dominating scattering processes and the signatures of different surface types. However, the overall net polarization of Earth depends strongly on the not so well known contributions of the different areas to the total signal. Therefore it is very desirable to have better observational data that constrain between the various model options.

Lunar earthshine observations are very attractive for investigating the intensity and polarization of the reflected light of the Earth because they provide the integrated scattered light signal from the whole planet Earth from the ground. However, for retrieving the real level of scattered intensity f_E and fractional polarization p_E of the Earth from the measured earthshine signals f_{es} and p_{es}, one also needs to consider the backscatter properties of the absorbing and depolarizing lunar surface.

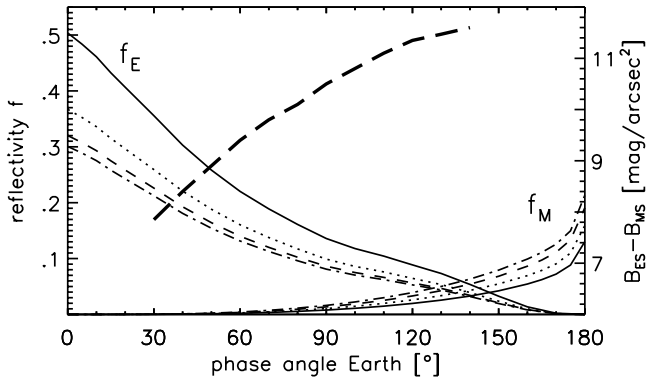

Fig. 1. Reflectivity of the Earth $f_E(\alpha_E, \lambda)$ and the Moon $f_M(\alpha_E, \lambda)$ for B (solid), V (dotted), R (dashed), and I (dash-dot). The thick dashed line is the difference of the surface brightness between earthshine $B_{es}(\alpha_E, \lambda)$ and moonshine $B_M(\alpha_E, \lambda)$ for the 400−700 nm pass band.

In addition, earthshine observations are very special because the Moon is a bright and large target for modern astronomical instrumentation and because the contrast between the bright crescent and the dark side of the Moon is very high. It is therefore not straightforward to disentangle the earthshine from the disturbing contributions of the variable atmospheric (and instrumental) stray light from the bright moonshine and of the twilight.

In this paper we describe new earthshine polarization measurements taken with an imaging polarimeter designed especially for earthshine observations. Our data cover Earth phase angles from 30° to 110° providing calibrated $p_{es}(\alpha)$ curves in the four broad-band filters B, V, R, and I for lunar maria and highlands, which are corrected for the stray light from the moonshine and the sky background. Section 2 describes our instrument and Sect. 3 our measurements, while Sect. 4 discusses the data reduction. The observational results are given in Sect. 5, and then we discuss in Sect. 6 our correction for the depolarizing effect of the lunar surface. The final polarization phase curves $p_E(\alpha, \lambda)$ for Earth, and the derivation of the polarization flux $p_E \times f_E$ and the Earth-Sun polarization contrast C_p are given in Sect. 7. The last section gives a summary and discusses the potential of earthshine polarization measurements.

2. Instrumentation

2.1. Instrument requirements

The (surface) brightness of the lunar earthshine, the moonshine, and the contrast between the bright and dark sides of the Moon are described in the literature and summarized in Fig. 1. The reflectivity of the Moon $f_M(\alpha_M, \lambda)$ is from Kieffer & Stone (2005) and plotted as a function of the phase angle of the Earth α_E using $\alpha_E = 180° - \alpha_M$. The reflectivity of the Earth $f_E(\alpha_E, \lambda)$ is from earthshine observations and model calculations by Pallé et al. (2003) for the pass band 400−700 nm. Due to the lack of multicolor earthshine observations the same shape for the reflectivity phase curve given by Pallé et al. (2003) is adopted for all colors and the curves for the different bands are just scaled with the factors derived from earthshine spectra from Arnold et al. (2002) as described in Sect. 7.4. Measurements of the surface brightness of the earthshine $B_{es}(\alpha, \lambda)$ and the moonshine $B_M(\alpha, \lambda)$ were derived from observations of fiducial patches of highland regions (see also Qiu et al. 2003) by Montañés-Rodríguez et al. (2007) for the pass band 400−700 nm and Earth phase angles between $\alpha_E = 30°-140°$. In Fig. 1 we adopt their waxing Moon

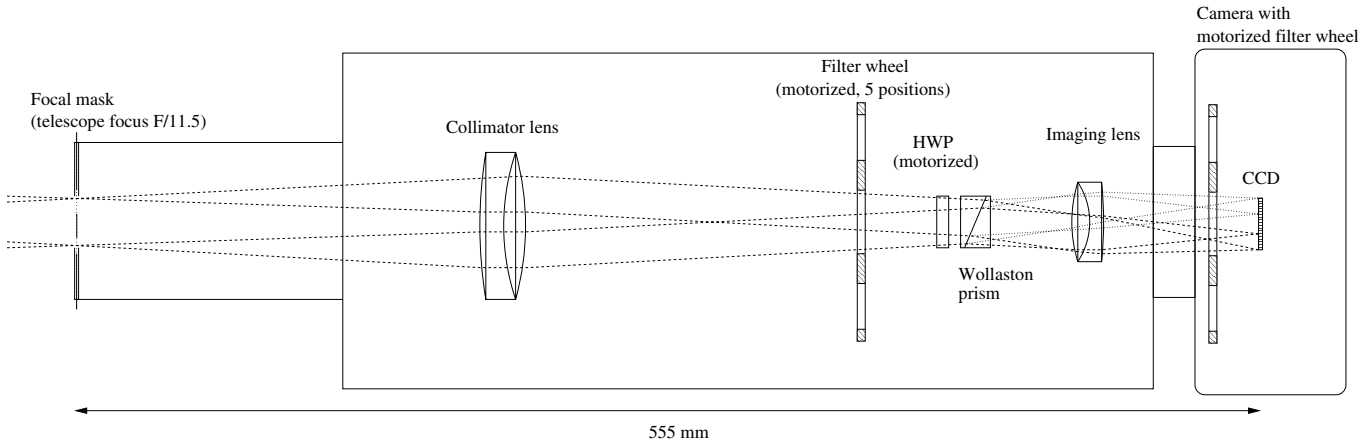

Fig. 2. Schematic overview of ESPOL with optical design and components drawn to scale. The focal mask is located in the focal plane of the 21 cm telescope.

results and derive the mean daily surface brightness contrast $B_{es}(\lambda) - B_M(\lambda)$ between the dark and the bright side of the Moon. For $\alpha = 90°$ (half moon) the surface brightness of the earthshine is 14.9 mag/arcsec^2. The difference between earthshine and moonshine ranges from 8−12 mag/arcsec^2 between $\alpha_E = 30°-140°$.

The surface brightness of the earthshine is highest for the new moon phase and decreases with the Sun-Earth-Moon phase angle α (Fig. 1). Observations for small α near new moon require daytime or twilight observations for which a correction for the sky light is impossible or difficult. For $\alpha \approx 45°$ an observational window of roughly 30 minutes with reasonably dark sky conditions becomes available after sunset or before sunrise for useful earthshine polarization measurements.

Observations during the night with much reduced sky background levels are possible for larger α, but the brightness of the moonshine due to the solar illumination increases rapidly (Fig. 1). At around $\alpha \approx 90°$ the contrast between moonshine and earthshine becomes greater than about 10^4 and the light scattering in the Earth atmosphere and the instrument becomes more and more a problem for earthshine observations particularly in the red where the moonshine is strong and the earthshine weak. The light from the twilight sky and the moonshine are both strongly polarized $p > 3\%$, and this needs to be considered for an accurate measurement of the earthshine polarization. The polarization of the moonshine is discussed in detail in Sect. 5.3.

2.2. The earthshine polarimeter

The EarthShine POLarimeter (ESPOL) measuring concept takes the background and stray light conditions for earthshine observations into account. The instrument allows imaging polarimetry of the entire Moon and the surrounding sky regions in order to measure the polarization signal of the weak earthshine on top of the strong stray light from the moonshine and/or the light contribution from the sky. ESPOL includes in addition exchangeable focal plane masks to block the light from the bright moonshine. The blocking of the bright crescent is required to allow for integrations of a few seconds without heavy detector saturation.

ESPOL is a dual-beam imaging linear polarimeter based on the rotating half-wave retarder plate and Wollaston polarization beam splitter concept. A schematic overview of the instrument is given in Fig. 2. The instrument includes a holder for exchangeable focal masks with different Moon-phase shapes to block the light from the bright lunar crescent in order to avoid heavy detector saturation. ESPOL uses a superachromatic $\lambda/2$ retarder plate on a motorized rotational stage for polarization beam switching and the selection of the Q and U polarization direction. The following Wollaston prism splits the light into the ordinary $i_{\parallel}$ and extraordinary $i_{\perp}$ beams with polarizations that are perpendicular to each other. Both beams, each with a field of view of $50' \times 40'$, are imaged on the same 3072×2048 pixel CCD detector with a pixel scale of 1.5 arcsec/pixel. For our measurements we used a pixel binning of 3×3 pixels, which reduced the spatial resolution to roughly 10 arcsec.

Color or neutral density filters with a diameter of 5 cm or 2 inches can be inserted into the five-position filter wheel located in the collimated beam or into the camera filter wheel, respectively. To optimally align the focal masks to the orientation of the bright lunar crescent, the mask holder can be rotated around the optical axis. In addition the whole instrument can be rotated around the optical axis to fix the zeropoint of the polarization direction to any desired orientation.

ESPOL was built in-house for low costs using equipment for amateur astronomers and standard polarimetric and optical components for the wavelength range of 360−860 nm. The instrument is attached to an equatorially mounted 21 cm Dall-Kirkham Cassegrain telescope. A thermo-electrically cooled SBIG-STL 6303E camera with integrated filter wheel and shutter is used as the CCD system.

Figure 3 illustrates the data format delivered by the CCD. Because of the large field of view and the use of simple optical components, the system shows some image distortion in the north-south direction where the Moon diameter between ordinary and extraordinary beam differs by about 5%. These distortions can be tolerated because we are not interested in high spatial resolution but in the fractional polarization of extended surface regions.

3. Observations

With ESPOL we measured the polarization of the earthshine for different phase angles and different wavelengths using a Bessell B, V, R, I filter set (Bessell & Murphy 2012). To minimize read-out overheads and detector noise the CCD was operated with 3×3 pixel binning providing a spatial resolution of about 10 arcsec, which is high enough for distinguishing mare and highland regions on the Moon. To minimize differential instrumental effects in the polarimetric signal the measurements

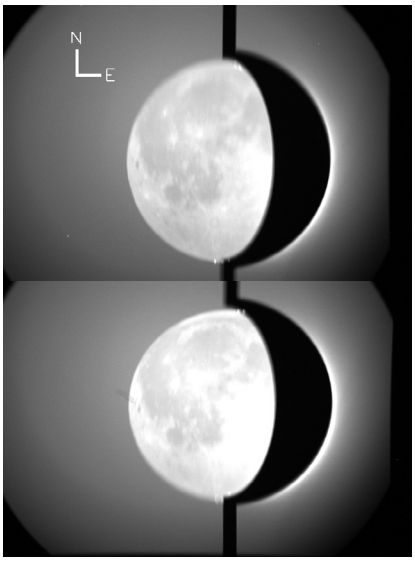

Fig. 3. ESPOL raw frame with the two polarization images $i_{\parallel}$ and $i_{\perp}$ of the earthshine on the Moon and the dark focal mask that blocks the light from the bright crescent.

have been performed in beam-exchange mode (Tinbergen 1996). Only the linear Stokes components Q/I and U/I are measured.

One polarimetric cycle consists of two measurements with half-wave plate positions 0° and 45° for Q/I and two measurements with positions 22.5° and −22.5° for U/I. Typical integration times per exposure were about 2−10 s per half-wave plate position so that one full cycle could be recorded in about one minute. This is fast enough to avoid problems with guiding drifts and strongly changing atmospheric conditions. To improve the signal-to-noise ratio (S/N) a series of about five to ten such datasets were typically recorded for each wavelength band during one observing night.

ESPOL was rotated for all our measurements, including standard stars, into the orientation of the plane Sun-Earth-Moon so that the Stokes $+Q$ direction is a polarization perpendicular to this plane and $-Q$ a polarization in this plane. The Stokes $\pm U$ directions are ±45° with respect to this plane. The alignment was done by eye by rotating the complete instrument until the crescent shaped focal mask completely blocked the moonlight, which led to an alignment accuracy of about $\Delta\theta = \pm 2°$. For instrument monitoring and calibration, additional polarimetric measurements of the moonshine and polarized/unpolarized standard stars, as well as darks and twilight flatfield calibrations were recorded during each observing night.

Our data were collected during two observing runs in March and October 2011. For the run in March the instrument was installed at the former Swiss Federal Observatory in Zurich at an altitude of 470 m above sea level. This run served mainly for first instrument testing and data with limited wavelength and phase coverage were obtained. Despite the nonoptimal observing location in the heart of the city, the data quality was good enough to be included in this study. For the second run, we moved the instrument to the former Arosa Astrophysical Observatory at an altitude of 2050 m located in the Alps of eastern Switzerland. This site provides a much darker sky and a much reduced level of light scattering in the Earth atmosphere allowing measurements of the earthshine polarization for larger phase angles.

Both observing runs cover phase angles for the waxing Moon only. For the March measurements the earthshine originates mainly in the Atlantic Ocean, the Pacific Ocean, and the American continent, while in October the earthshine was due to reflected light from South America and the Atlantic Ocean. Table 1 gives an overview of the observed phase angles of our measurements, the used filters, and the number of polarization cycles for each filter.

Table 1. Observing log.

Observing date	Phase	Filters	# pol. cycles
07.03.2011	31.5°	V	11
08.03.2011	42.5°	B, V, R	3, 9, 2
11.03.2011	75.5°	B, V, R	8, 19, 4
02.10.2011	73.0°	B, V, R, I	1, 3, 4, 4
03.10.2011	85.5°	B, V, R, I	5, 5, 4, 5
04.10.2011	98.0°	B, V, R, I	16, 15, 21, 6
05.10.2011	109.5°	B, V, R, I	8, 8, 10, 8

Notes. The number of polarization cycles refer to the different filters taken for this date.

4. Data reduction

4.1. Polarimetric reduction

Figure 3 shows a typical ESPOL raw frame with the ordinary $i_{\parallel}$ and extraordinary $i_{\perp}$ beams from the Wollaston showing the earthshine on the Moon in two opposite polarization directions. The bright crescent is blocked by the focal mask in order to suppress stray light in the instrument and to avoid disturbing detector saturation.

In the first data reduction step, the raw images were dark-subtracted before the two opposite polarization images $i_{\parallel}$ and $i_{\perp}$ for all half-wave plate orientations (0°, 45°, 22.5°, and −22.5°) were cut out and aligned. Then the fractional Stokes parameter Q/I images were calculated according to the beam-exchange method described in Tinbergen (1996):

$$q = \frac{Q}{I} = \frac{R-1}{R+1} \quad \text{with} \quad R^2 = \frac{i_{0,\parallel}/i_{0,\perp}}{i_{45,\parallel}/i_{45,\perp}}, \tag{3}$$

where the first index of the image i refers to the $\lambda/2$ retarder orientation, and $\parallel$ and $\perp$ indicate the two opposite polarization states from the ordinary and extraordinary beams of the Wollaston prism.

The corresponding intensity images are calculated by

$$I_Q = 0.5\,(i_{0,\parallel} + i_{0,\perp} + i_{45,\parallel} + i_{45,\perp}). \tag{4}$$

The polarization and intensity images for the Stokes U measurements are determined in the same way but using the frames taken with +22.5° and −22.5° retarder positions.

In the differential polarization measurements, effects like the spatial variations of the system throughput, detector pixel-to-pixel sensitivity differences, and temporal changes between individual measurements are compensated to first order with the used double ratio, without any application of a flatfielding correction. Therefore, flatfielding was only applied on the intensity image I_Q described in Eq. (4) using an intensity flatfield image produced in the same way.

As described above there are some image distortions due to the large field of view and the relatively simple optical setup. These differential distortions between the ordinary $i_{\parallel}$ and extraordinary $i_{\perp}$ beams disappear almost entirely in the double ratio method because images from both beams are in the nominator and denominator of that ratio. This first-order cancellation effect

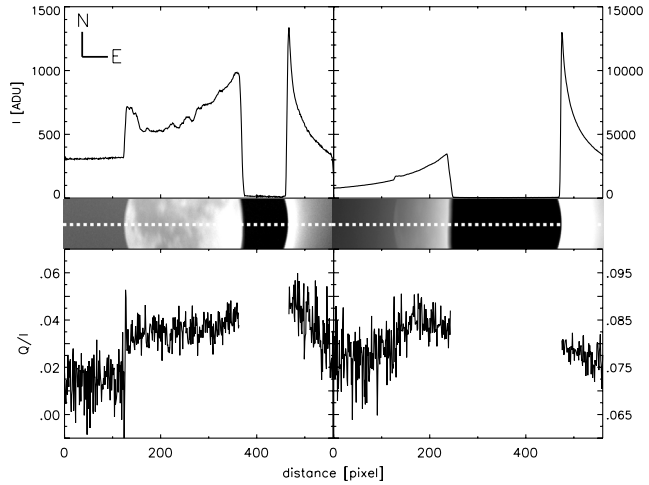

Fig. 4. Lunar west-east intensity (*top*) and polarization (*bottom*) profiles in the *B* band for phase 42.5° and 98.0° with a low (*left*) and high (*right*) stray light contribution from the moonshine, respectively. The panel in the *middle* shows the corresponding stripe of the intensity images. The profiles were extracted from 10 pixel wide regions as indicated by the dashed lines in the *middle panel*.

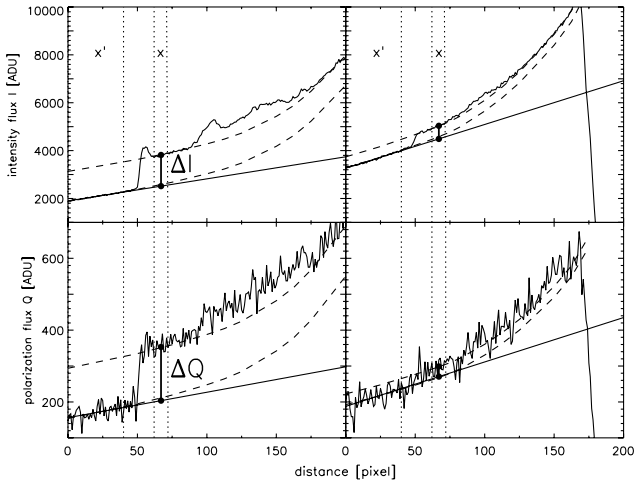

Fig. 5. Measuring the earthshine signals ΔI, ΔQ for relatively low (phase 73°, region #1, filter *B*) and high (phase 98°, region #1, filter *R*) moonshine levels with the background x' and measuring regions x indicated. The dashed lines illustrate the guessed level of the background (mainly stray light) and background plus constant earthshine regions (reflected from maria). The full line is the linear extrapolation of the measured background from the x' to the x region.

is not present in the summed intensity images and leads to some spatial smearing. Therefore the limb of the Moon is not sharp in the intensity image but on the more relevant larger scales, that is for identifying extended mare or highland regions, the image distortions are negligible. Nonetheless we have considered in our data analysis that small scale features may be affected by image distortion effects and the associated alignment inaccuracies.

The polarimetric properties of ESPOL were tested with observations of zero polarization standard stars β Tau, β UMa, γ Boo, (Turnshek et al. 1990), and Vega (Bhatt & Manoj 2000), which show that the instrumental polarization is ≤0.5% in all filters. From the polarized standard stars HD 21291, 9 Gem, ϕ Cas, 55 Cyg (Hsu & Breger 1982), we deduced a polarimetric efficiency above 98% and checked the zero point of the polarization direction.

4.2. Extracting the earthshine polarization

We are interested in the measurement of the fractional polarization of the earthshine $(Q/I)_{\rm es}$, which needs to be extracted from our data. Our observations show the contributions of three intensity components

$$I_{\rm tot} = I_{\rm es} + I_{\rm M} + I_{\rm sky}$$

from the earthshine (es), the scattered light from the moonshine (M), and the sky (see Fig. 4). In our images it is rather easy to distinguish these components, assuming that the sky is essentially constant over the whole field of view. The location of the earthshine is well defined, and its intensity lies in a restricted range between the intensities of dark maria and bright highlands. The scattered light intensity from the moonshine has a more complex geometry. It is increasing rapidly toward the bright crescent, which is covered in our data by the occulting mask.

The signatures of the three components can also be recognized in the fractional polarization W-E cuts extracted from the Q/I images shown in Fig. 4. The *B*-band observation for phase 42.5° shows a significant sky contribution from the twilight. The sky polarization is about 1.5% on the west side of the Moon, and the earthshine plus sky polarization is about 3.5%. The polarization of the moonshine is slightly higher (~4.5%) as can be seen near the east side of the occulting mask where the scattered light of the moonshine dominates. For phase 98° the scattered moonshine dominates strongly with a polarization of about 8%. The fractional polarization is just slightly enhanced at the position of the earthshine. The (Q/I)-images consist of the following contributions

$$\left(\frac{Q}{I}\right)_{\rm tot} = \frac{Q_{\rm es} + Q_{\rm M} + Q_{\rm sky}}{I_{\rm tot}}. \quad (5)$$

Because of our definition of the $\pm Q$-directions perpendicular and parallel to the scattering plane, the U/I polarization is essentially zero (≈±0.5%) and dominated by noise.

After some investigation we defined a procedure for extracting the fractional earthshine polarization $(Q/I)_{\rm es}$, which also provides good results for large-phase angles, and the *I* filter for which the signal is weak and/or the stray light from the moonshine is very strong. For small phase angles, the earthshine signal is strong and the measurement is easy. The basic idea is to measure the signal of the earthshine on top of the "background signal" in the $I_{\rm tot}$ frame and the $Q_{\rm tot}$ frame where $Q_{\rm tot} = (Q/I)_{\rm tot}\, I_{\rm tot}$. The "background signals" (bg) are just the sum of the contributions of the sky and the moonshine $I_{\rm bg} = I_{\rm sky} + I_{\rm M}$ and $Q_{\rm bg} = Q_{\rm sky} + Q_{\rm M}$. For this we extract radial cuts and extrapolate the background signal from the region x' outside to a location x inside the lunar disk ($I_{\rm bg}(x')$, $Q_{\rm bg}(x') \rightarrow I_{\rm bg}(x)$, $Q_{\rm bg}(x)$) where we measure the earthshine + background level. The final signal is then

$$\left(\frac{Q}{I}\right)_{\rm es} = \frac{\Delta Q}{\Delta I} = \frac{Q_{\rm bg+es}(x) - Q_{\rm bg}(x)}{I_{\rm bg+es}(x) - I_{\rm bg}(x)}. \quad (6)$$

This procedure is illustrated in Fig. 5, for two cases. The first is a strong and clear earthshine signal typical of phase angles $\alpha < 109°$ in the B, V filters and phase angles $\alpha < 98°$ in the *R* filter. The large majority of our data are of this kind. The other case is typical of phase angles $\alpha \geq 98°$ in the *R* and *I* band filter

Table 2. Fractional polarization values $(Q/I)_{es}$ for the earthshine from the mare and highland regions of all our measurements and corresponding typical statistical 1σ uncertainties Δ_{noise}.

Date (2011)	Phase (Sun-Earth-Moon)	Q/I (highland) [%]				Q/I (mare) [%]			
		B	*V*	*R*	*I*	*B*	*V*	*R*	*I*
07.03	31.5°	–	1.5	–	–	–	2.3	–	–
08.03	42.5°	4.0	3.4	2.3	–	5.4	4.6	3.5	–
02.10	73.0°	8.7	6.1	4.0	2.5	11.9	8.1	5.3	2.9
11.03	75.5°	9.7	6.9	4.5	–	12.9	8.7	6.4	–
03.10	85.5°	9.4	6.9	4.8	2.9	12.7	8.6	5.7	2.7
04.10	98.0°	9.1	6.9	5.0	3.4	11.9	8.6	6.1	3.7
05.10	109.5°	7.7	5.7	4.2	3.1	11.1	8.4	5.9	8.6[a]
Statistical 1σ uncertainty Δ_{noise} [%]		0.2	0.2	0.2	0.2	0.4	0.3	0.3	0.3
Fit parameter q_{max} [%]		9.4	7.0	4.7	3.0	12.7	9.0	6.1	3.2
Stddev of data from fit σ_{d-f} [%]		0.22	0.13	0.10	0.21	0.24	0.13	0.22	–
Polarization efficiency ϵ [%][b]		36.6	34.3	32.7	30.7	54.3	50.8	48.5	45.6
ϵ corrected $q_{max,corr}$ [%]		25.8	20.3	14.4	9.6	23.4	17.8	12.6	6.9

Notes. Also given is the fit parameter for $q_{max}\sin^2(\alpha)$ derived in Sect. 5.2 and the standard deviation of the data points from the fit σ_{d-f}. The polarization efficiencies $\epsilon_{\#1}$ and $\epsilon_{\#2}$ are derived in Sect. 6 and the depolarization corrected values $q_{max,corr}$ are given. [(a)] Value affected by systematic errors due to high stray light level (see text). [(b)] The uncertainty of ϵ is mainly a systematic offset estimated to be $\Delta\epsilon = \pm 3\%$ (see text).

for which the stray light from the moonshine dominates strongly. The Q signal from the earthshine is still above but close to the measuring limit. Also given are fits to the background, which in these cases mainly consist of the moonshine plus a constant earthshine level fitted to the mare regions. The use of a linear extrapolation of the background in the x' region for the background correction of the total earthshine plus background signal measured at x seems reasonable (see also Qiu et al. 2003; Hamdani et al. 2006).

We have investigated more complex background/straylight correction procedures, e.g. using three-parameter exponential fits, but they did not agree better than the linear extrapolation. Important for the accuracy of the earthshine measuring process is to select areas close to the western limb but not exactly at the limb because image alignment uncertainties of the polarimetric data reduction can create disturbing spurious features at the limb. The limb is also not a good measuring region because of the extreme incidence and reflection angles (near 90°) with respect to the large-scale surface normal that represents a situation that is not explored well for its backscattering properties.

All our data show that the differences between the lunar dark mare and bright highland regions are significant when determining the intensity and polarization of the backscattered earthshine. Therefore it is important to carry out separate measurements for these two main lunar surface types. Because of the strong albedo dependence (see Sect. 6), it is important that a chosen measurement field on the Moon does not have strong albedo variations. Under these terms we selected one mare field #1 in the Oceanus Procellarum area and one highland field #2 between Mare Humorum and the Moon's limb as indicated in Fig. 6. Both fields are close to the western limb far away from the bright lunar side. They are available for measurements at all phase angles α when taking increasing stray light and the lunar libration into account. Therefore, for both fields a consistent data reduction could be carried out.

For both fields ten radial I and Q profiles separated by one degree were extracted, and ΔI and ΔQ were determined as described above. Table 2 gives the obtained $(Q/I)_{es}$ polarization values from both fields, which are also plotted in Fig. 7 as phase curves, together with the statistical 1σ error bars Δ_{noise}.

As long as the S/N is sufficiently high, the linear extrapolation method is robust. The total uncertainty for the obtained

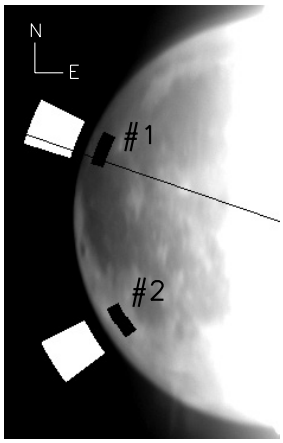

Fig. 6. Selected mare (#1) and highland (#2) fields used for the earthshine measurements, together with their background regions (white areas).

fractional polarization of the earthshine for a highland or mare region at a particular date can be described by the statistical noise plus a predominantly positive systematic offset $\Delta(Q/I)_{es} = \Delta_{syst} \pm \Delta_{noise}$.

The statistical 1σ uncertainty Δ_{noise} is small (<0.3%). This follows from the scatter of the obtained values from different extraction cuts of the same day and includes random noise, but also hard to quantify systematic effects owing to small image drifts on the detector, changing stray light levels of the moonshine related to unstable atmospheric conditions, and perhaps other unidentified effects.

For observations with very small earthshine signals (i.e., at large phase angles and/or strong stray light of the moonshine), the linear extrapolation of the background introduces a systematic overestimate Δ_{syst} of the result. This is because the moonshine-dominated stray light background increases with an upward curvature toward the illuminated crescent. For the B, V, and R measurements at phase angles <100° this offset is negligible or small (<0.5%); however, in the I band filter at phase angle 109.5° the systematic offset clearly dominates and the mare I band result for 109.5° is no longer useful (see Fig. 7). For this reason we disregard the mare I band result at 109.5°.

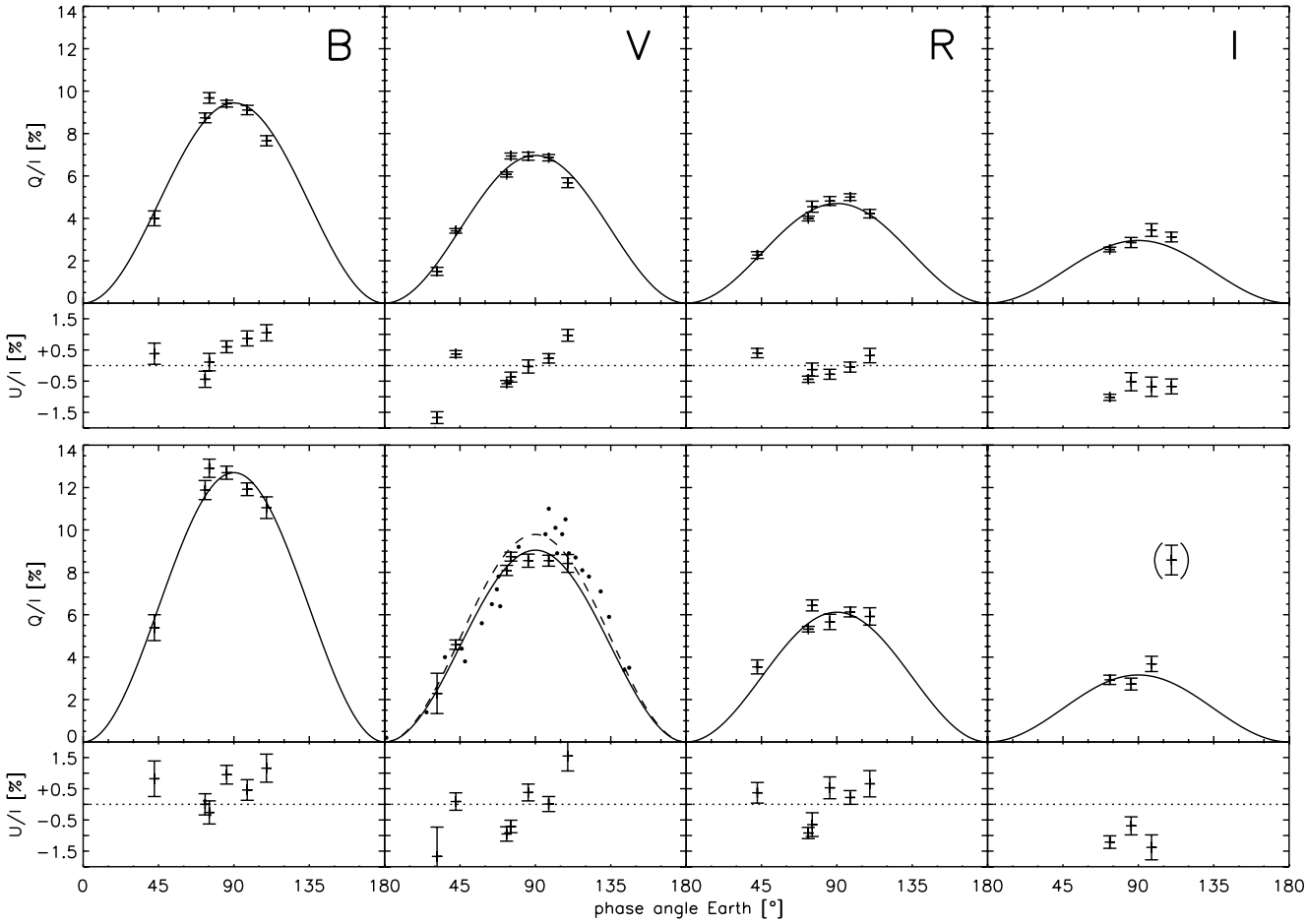

Fig. 7. Fractional polarization Q/I and U/I of the earthshine measured for highland (*top*) and mare regions (*bottom*) for the four different filters B, V, R, and I (*left to right*). The solid curves are $q_{\max} \sin^2$ fits to the data. The error bars give the statistical 1σ noise $\Delta_{\rm noise}$ of the data, whereas the mare I band data at phase angle 109.5° are additionally affected by a substantial systematic offset $\Delta_{\rm syst} > 0.5\%$. The dots in the V panel for the mare region indicate the measurements of Dollfus (1957) and a corresponding $q_{\max} \sin^2$ fit (dashed line) is also given.

5. Earthshine polarization results

5.1. Data

The results for the fractional earthshine polarization Q/I measured in the Bessell B, V, R, and I bands are presented in Table 2 and Fig. 7. The plots in Fig. 7 also include the U/I data points and the estimated statistical 1σ uncertainties of the individual data points $\Delta_{\rm noise}$. The mare V band panel also shows the measurements by Dollfus (1957), which are in good agreement with our data.

Our earthshine data show a tight correlation between the polarization taken simultaneously for the highland and mare regions. Independent of color filter and phase angle, the polarization for the mare region is a factor of 1.30 ± 0.01 higher than for the highland region as illustrated in Fig. 8.

Tight correlations are also found between different colors taken for the same observing date. When we plot the polarization $(Q/I)_{\rm es}$ in the V, R, and I bands versus the polarization in the B band (Fig. 9), we find that the ratios are independent of $\alpha_{\rm E}$. We get 0.72 ± 0.02, 0.49 ± 0.02, and 0.28 ± 0.05 for the ratios of the polarization between the V and B bands, R and B bands, and I and B bands respectively. Therefore, we conclude that to first order we can assume the same shape for the polarization phase curve for all wavelengths.

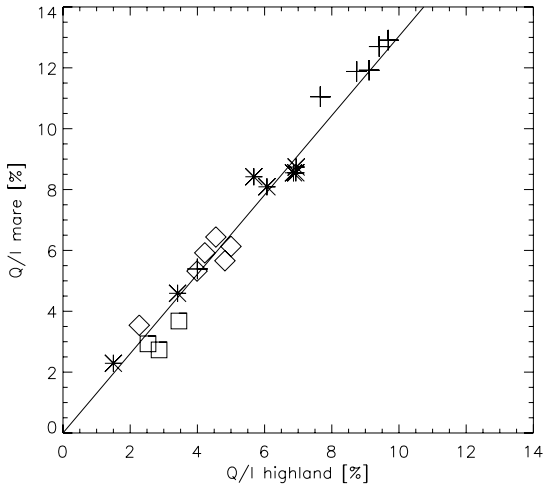

Fig. 8. Correlation between the fractional polarization for mare and highland regions measured simultaneously. The different symbols indicate the colors $B(+)$, $V(*)$, $R(\diamond)$, and $I(\square)$. The line shows the derived proportionality factor 1.30 ± 0.01.

5.2. Fits for the phase dependence

The phase dependence of the earthshine polarization looks symmetric and can be well fitted with a simple $q_{\max} \sin^2(\alpha)$ curve.

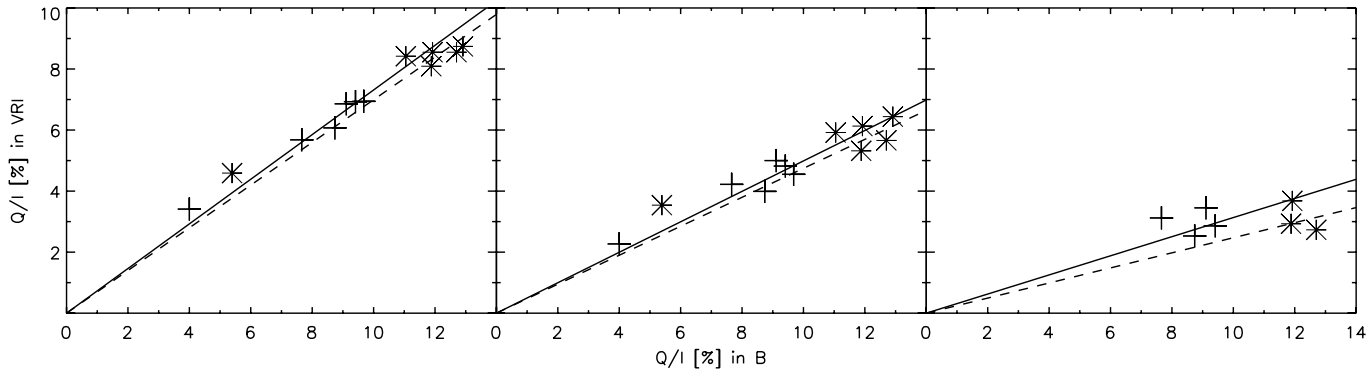

Fig. 9. Fractional polarization of the earthshine reflected at highland (+) and mare (∗) regions in V, R, and I bands (*left to right*) with respect to the B band. The lines indicate linear fits both for highland (solid) and mare (dashed) data separately.

The model simulations by Stam (2008) for Earth-like planets also support phase curves $q_{\max} \sin^p(\alpha)$. She calculates polarization phase curves assuming a range of surface types (e.g., forest-covered areas with Lambertian reflection or dark ocean with specular reflection) and cloud coverages. We find that the broad shape of her model phase curves can be well fitted by curves $\sim q_{\max} \sin^p(\alpha + \alpha_0)$ with $p \approx 1.5{-}3$ and $\alpha_0 \approx 0°{-}10°$.

Furthermore, she finds characteristic features at low phase angles owing to the rainbow effect and negative polarization at large phase angles caused by second-order scattering. We cannot assess the presence of such features because of the coarse phase sampling of our data.

Besides the $q_{\max} \sin^2(\alpha)$ curve we also tried functions with more free parameters to fit the data, such as using a curve like $q_{\max} \sin^p(\alpha + \alpha_0)$, varying the exponent p between values of 1.5−3 and by introducing a phase shift α_0. However, such fits do not provide a significantly better match to the data. Because our data predominantly cover phase angles around quadrature the shape of the phase curve is not very well constrained.

The derived $q_{\max}$ fit parameters for the different phase curves are given in Table 2, along with the standard deviation of the data points from the fit $\sigma_{\mathrm{d-f}}$. For Q/I the typical $\sigma_{\mathrm{d-f}}$ is ≈0.2% in good agreement with the typical 1σ uncertainty of the individual data points Δ_{noise}. The standard deviation of the derived U/I values from the expected zero-value is only slightly higher and typically ≈0.3%, indicating that the instrument alignment with respect to the Sun-Earth-Moon plane was excellent (see Sect. 3). The U signal is at the level of the measurement noise $|U| \approx \Delta_{\mathrm{noise}}(U)$. Therefore one should not use the normalized total polarization $\mathrm{p} = \sqrt{(Q/I)^2 + (U/I)^2}$ because the square in this formula introduces systematic errors. However, we estimate that the impact of U/I to the total polarization p is less than ±0.05%. Therefore we use $p \cong Q/I$ and neglect the U component in the subsequent discussion.

5.3. The moonshine polarization

As a check of our polarimetry we can compare the polarization of the stray light from the moonshine with values from Coyne & Pellicori (1970) and Dollfus & Bowell (1971). Forward scattering in the Earth atmosphere with scattering angles less than a few degrees does not introduce a significant polarization effect. Therefore, we can assume that the polarization of the lunar stray light $(Q/I)_{\mathrm{M}}$ represents the polarization of the bright lunar crescent well. For areas just east of the Moon close to the focal mask (see Fig. 4) the scattered moonshine dominates strongly. There we can neglect the contribution of the sky background $(Q/I)_{\mathrm{sky}}$ and assume that $(Q/I)_{\mathrm{bg}} \approx (Q/I)_{\mathrm{M}}$.

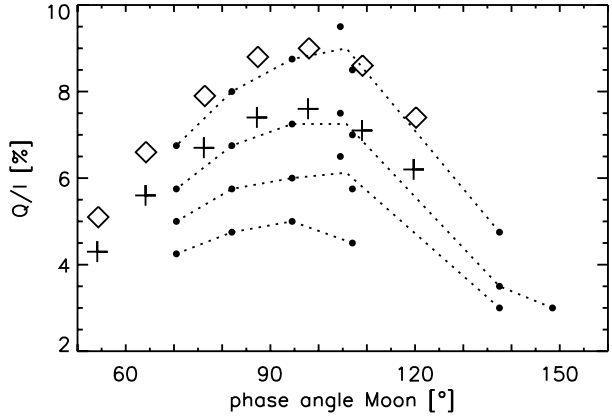

Fig. 10. Measured polarization of the lunar stray light near the focal mask in the B, V, R, and I filters (from *top to bottom* by filled dots and dashed lines). Also indicated are the polarization values given by Coyne & Pellicori (1970) for the disk integrated moonshine of the waxing Moon in their B' (⋄) and G_{m} bands (+).

Figure 10 compares our results with the waxing Moon values given by Coyne & Pellicori (1970). They used different filters but their B' and G_{m} bands ($\lambda_{\mathrm{eff}}[\mu\mathrm{m}] = 0.45, 0.53$) are close to our B and V bands, and the good agreement with our data underlines the consistency of our polarimetric data reduction.

Unfortunately, Coyne & Pellicori (1970) used no red filters, but the scaled G_{m} phase curve fits our R and I band data also well if scaling parameters of 0.80 and 0.65 are used. This is in good agreement with the wavelength dependency of the maximum degree of polarization $P_{\max}$ of the whole Moon presented in Dollfus & Bowell (1971):

$$P_{\max,\lambda_1}/P_{\max,\lambda_0} = (\lambda_1/\lambda_0)^{-1.137}. \quad (7)$$

With this formula we obtain color ratios of $q(R)/q(G_{\mathrm{m}}) = 0.81$ and $q(I)/q(G_{\mathrm{m}}) = 0.64$ for the Moon polarization in good agreement with the above scaling parameters derived from our stray light data.

6. A correction for the depolarization due to backscattering at the lunar surface

The polarized light from the Earth is depolarized by the backscattering at the particulate surface of the Moon. We express this effect as polarization efficiency ϵ, to describe the fraction of

linear polarization preserved. We simplify the treatment by only considering the Q linear polarization direction perpendicular and parallel to the scattering plane Sun-Earth-Moon. Then the polarization efficiency is

$$\epsilon = \frac{(Q/I)_{\rm es}}{(Q/I)_{\rm E}},$$

where $(Q/I)_{\rm E}$ is the Earth polarization. The polarization efficiency $\epsilon(\lambda, a_\lambda)$ depends on the wavelength and the surface albedo. We neglect the phase dependence because the scattering angle is always $179° \pm 0.5°$.

The depolarization of the lunar surface has already been investigated by Lyot (1929) and Dollfus (1957). They measured the depolarization due to backscattering at volcanic ashes and fines, which were used as proxies for the lunar soil. They found a well-defined anticorrelation between albedo and polarimetric efficiency.

Most important for determining $\epsilon(\lambda, a)$ are the albedo and polarization measurements for the reflection from several Apollo lunar soil samples by Hapke et al. (1993, 1998). They illuminated eight samples under an inclination of five degrees (to avoid specular reflection) with 100% polarized blue and red light and measured the ratio of $I_\perp/I_\parallel$ for phase angles 1° (∼backscattering) to 19° or scattering angles of 179° to 161°. The results for the linear polarization ratio are presented in Hapke et al. (1993) in graphical form, and we extracted the data for phase angle 1° and derived the polarization efficiency ϵ. The normal albedos are only given for a phase angle of 5° (Hapke et al. 1993, Table 1), and we converted them into earthshine backscatter albedos corresponding to 1° phase angle by applying a conversion factor of 1.25 ± 0.05. We derived this factor from albedo phase curves presented in Velikodsky et al. (2011) where they give a comprehensive summary of the results of various independent photometric observations of the Moon including their own, Clementine data, and ROLO data.

The samples from Hapke et al. (1993) include five low albedo samples $a_{\rm red} \approx 0.09$–0.13 representative of maria, two higher albedo samples $a_{\rm red} \approx 0.15$–0.19 representative of highlands, and one atypical, extremly high albedo sample with normal albedo $a_{\rm red} > 0.35$. This sample with NASA number 61221 was taken from white material at the bottom of a trench (see The Lunar Sample Compendium[1]), and we therefore treat this sample as special case in our analysis.

Figure 11 shows the polarization efficiencies for the measurements of Hapke et al. (1993) as a function of the 1°-albedo for a blue wavelength (λ = 442 nm) and a red wavelength (λ = 633 nm). The figure nicely illustrates the clear anticorrelation between albedo a and polarization efficiency ϵ.

We consider now the backscatter properties of the lunar samples in more detail. All samples, except 61221, show a very similar color dependence in their albedo with $a_{\rm red}/a_{\rm blue} = 1.35$ ($\sigma = 0.05$). This agrees with the spectral variation of the mean lunar albedo $\bar{a}$ from Dollfus & Bowell (1971) (see also Gehrels et al. 1964, Table XIII; and Velikodsky et al. 2011, Table 2) described by

$$\log \bar{a} = 0.83 \log \lambda[\mu{\rm m}] - 0.80. \quad (8)$$

Inserting the wavelengths of the Hapke et al. (1993) measurements into this formula yields $\bar{a}_{\rm red}/\bar{a}_{\rm blue} = 0.108/0.0805 = 1.34$, in very good agreement with the albedo ratio derived above for the lunar samples.

[1] http://curator.jsc.nasa.gov/lunar/compedium.cfm

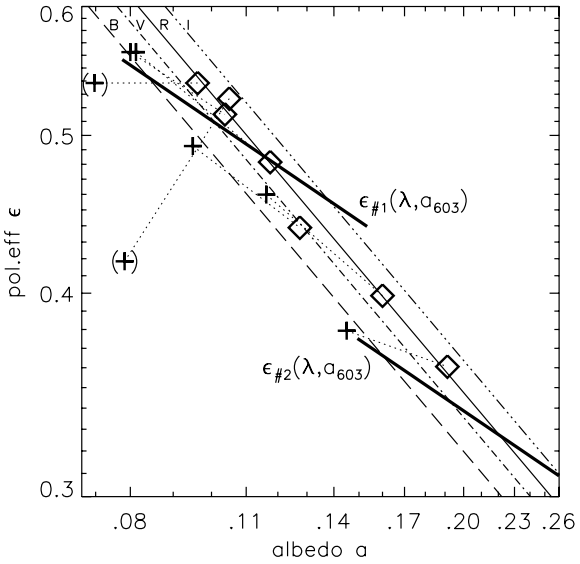

Fig. 11. Linear polarization efficiency as function of the normal albedo at 1° (Eq. (9)) for the *B* (dashed), *V* (dash-dot), *R* (solid), and *I* (dash-dot-dot) band. More information about the fit procedure to the Hapke et al. (1993) samples in the red (⋄) and the blue (+) is given in the text. Measurements of the same sample are connected by dotted lines. The thick black lines show the derived wavelength and albedo-dependent polarization efficiencies for our two measurement areas #1 and #2 (Fig. 6).

For most samples the polarization efficiency is slightly higher (in one case equal) in the blue than in the red. There is one notable exception, which is sample number 79221. Although the albedo of sample 79221 is lower in the blue than in the red, its polarization efficiency is not higher in the blue as is the case in all other samples. Also when looking into reflectivity studies for this sample (e.g. Noble et al. 2001), it is not clear why this sample could behave differently in its depolarization properties than other maria soils. Therefore, we treat sample 79221 as an exception.

If we disregard sample 79221, then the remaining six samples have an average color dependence for their polarization efficiency ratio of $\epsilon_{\rm red}/\epsilon_{\rm blue} = 0.91$ ($\sigma = 0.05$). Including sample 79 221 gives a mean ratio of 0.96 but a standard deviation that is significantly higher with 0.14.

Based on these backscatter measurements of lunar samples, we derived a two-dimensional linear fit for the polarization efficiency $\log \epsilon$ as function of $\log a_{603}$, the albedo at 603 nm, and $\log \lambda$ for the wavelength

$$\log \epsilon(\lambda, a_{603}) = -0.61 \log a_{603} - 0.291 \log \lambda\,[\mu{\rm m}] - 0.955. \quad (9)$$

For this fit the wavelength dependence of the albedo has been assumed to follow Eq. (8), and it was normalized to 603 nm. By fitting the red data points, we find the logarithmic slope -0.61 ± 0.04 between the polarization efficiency ϵ and the albedo $a_{\rm red}$, which we also adopted for the blue data points. Finally, by fitting over the red and blue points separately, we determined the other two parameters −0.291 and −0.955. The resulting relation for the linear polarization efficiency as a function of the normal albedo at 1° is shown in Fig. 11 for the *B*, *V*, *R*, and *I* bands.

For deriving the albedos of our measurement regions we used the results of Velikodsky et al. (2011), who present maps of lunar apparent and equigonal albedos at phase angles 1.7°–73° at wavelength 603 nm. We extrapolated their results to a phase angle of 1° and get albedos $a_{\#1}$(603 nm) = 0.11 ± 0.01

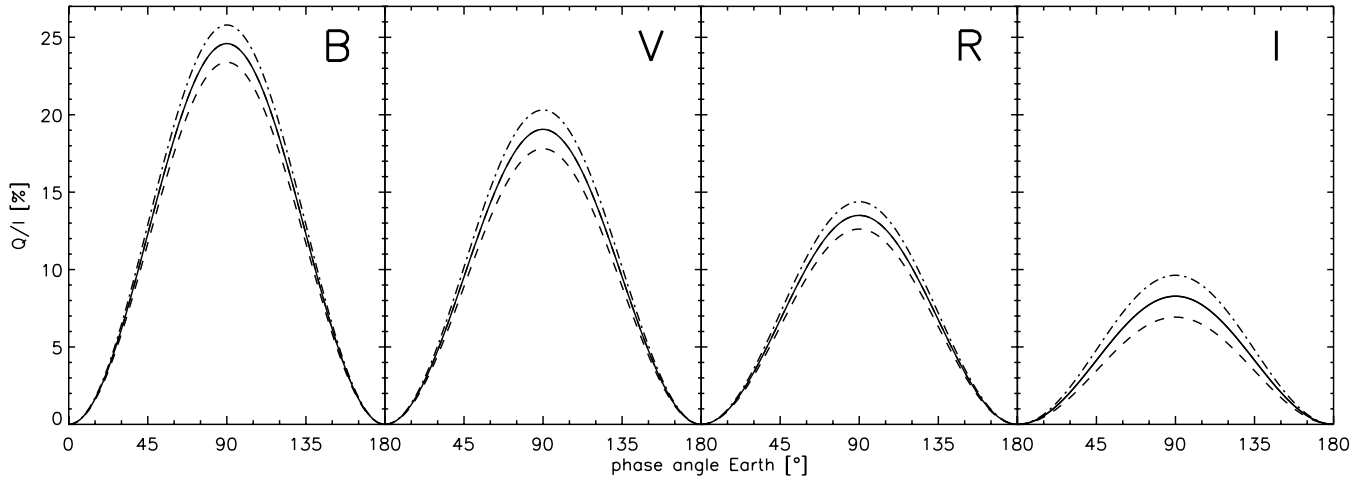

Fig. 12. Depolarization-corrected polarization phase curves of Earth in the B, V, R, and I bands. The solid line indicates the mean of the mare (dashed) and highland (dash-dot) results based on the polarization efficiency correction derived in this work.

and $a_{\#2}(603\ \mathrm{nm}) = 0.21 \pm 0.01$. The resulting polarization efficiencies $\epsilon_{\#1}(\lambda, a_{603})$ and $\epsilon_{\#2}(\lambda, a_{603})$ are listed in Table 2 for the B, V, R, and I bands and shown in Fig. 11 giving the $\epsilon(\lambda, a_{603})$ fits. Overall we estimate the uncertainty of the derived polarization efficiency to be $\Delta\epsilon \approx \pm 3\%$.

The main uncertainty of this derivation stems from the uncertainty in the above-mentioned albedo conversion from $\alpha = 5°$ into albedos corresponding to 1° phase angle where the conversion factor 1.25 ± 0.05 leads to an uncertainty of the polarization efficiency of about $\Delta\epsilon = \pm 1.5\%$. To significantly improve the determination of ϵ accurate lunar albedo maps for backscatter geometry are required. This is because backscattering by ≈1°, is strongly influenced by the opposition effect of the lunar surface, that is a steep brightness surge which comes from coherent backscattering and shadow hiding (e.g. Shkuratov et al. 2011, and references therein). In addition to that, the Hapke et al. (1993, 1998) sample might not be representative of the surface properties of the Moon.

The logarithmic slope -0.61 ± 0.04 is better constrained for the low-albedo samples, and it introduces an uncertainty $\Delta\epsilon = \pm 1\%$ toward the higher albedo samples. Moreover, the logarithmic relation might not be valid over the complete albedo range between $a_\lambda = 0.09$–0.19, so two slopes, one for the maria and one for the highlands, might be necessary. However, based on the available samples, this is not obvious, and one log fit may not be the best representation of the data. More direct measurements of the polarization efficiency of lunar backscattering are required to reduce this source of uncertainty.

7. Polarization of planet Earth

7.1. Fractional polarization derived from the earthshine

In Fig. 12 we present the depolarization-corrected polarization phase curves of planet Earth in the B, V, R, and I bands, and the corresponding corrected fit parameters $q_{\mathrm{max,corr}}$ are listed in Table 2. For the B band we obtain a maximum polarization of about 25% that decreases with wavelength to about 8% in the I band. For perfect measurements and perfect polarization efficiency corrections, the same Earth polarization $q_{\mathrm{max,corr}}$ values should be obtained for the mare and highland regions. We note that the corrected highland results are systematically higher than the mare results by a factor of about 1.1 for the B, V, R bands and 1.4 for the I band. This also reflects the uncertainty in our determination of the polarization efficiency of backscattering at the Moon $\Delta\epsilon \approx \pm 3\%$ derived in Sect. 6.

7.2. Comparison with previous measurements

In Fig. 7 we compare our earthshine measurements with the pioneering study of Dollfus (1957), who obtained his data with visual observations using a "fringed-field polariscope". The agreement with our V band phase curve for the mare region is excellent. If we apply $q_{\max} \sin^2$ fits (see Sect. 5.2) to both data sets, the quadrature signals only differ by 0.8%. The small deviations between Dollfus (1957) and us can be explained by different mare regions that were observed and the expectedly non-equal effective wavelengths of the two completely different types of measurements. For one night at $\alpha \approx 100°$, Dollfus (1957) also reports the earthshine polarization in two filters, namely $p = 5.4\%$ for 0.55 μm (V' band) and 3.5% for 0.63 μm (R' band). The ratio $p_{V'}/p_{R'} = 1.54$ is again in good agreement with our polarization ratio $q_{\mathrm{max},V}/q_{\mathrm{max},R} = 1.47$. This indicates that the filters used by Dollfus (1957) must match our filter pass bands quite well.

The spectral dependence of the earthshine polarization observed with a spectral resolution of 3 nm was recently published by Sterzik et al. (2012). These sensitive spectro-polarimetric data reveal weak, narrow features of the Earth due to O_2 and H_2O on a smooth polarization spectrum decreasing steadily from the blue toward longer wavelengths. They present measurements for two epochs with phase angles $\alpha = 87°$ for a waning moon phase and $\alpha = 102°$ for a waxing moon phase. For the waning moon case they obtained an earthshine polarization of about $p_B = 12.1\%$ in the B band, $p_V = 7.7\%$ in V, $p_R = 5.6\%$ in R, $p_I = 3.9\%$ in I, and a significantly higher polarization for the waxing moon phase with $p_{\mathrm{B}} = 16.6\%$, $p_V = 9.7\%$, $p_R = 8.0\%$, and $p_I = 6.7\%$, as plotted in Fig. 13. Unfortunately, it is not clear whether they measured the backscattering from maria or highlands. Sterzik et al. (2012) attribute the polarization differences between the two epochs mainly to intrinsic differences in the polarization of Earth because the earthshine stems from different surface areas and were taken for days with different cloud coverage. Considering our polarization values for highlands and maria, then it could be possible that the differences measured by Sterzik et al. (2012) are at least partly due to

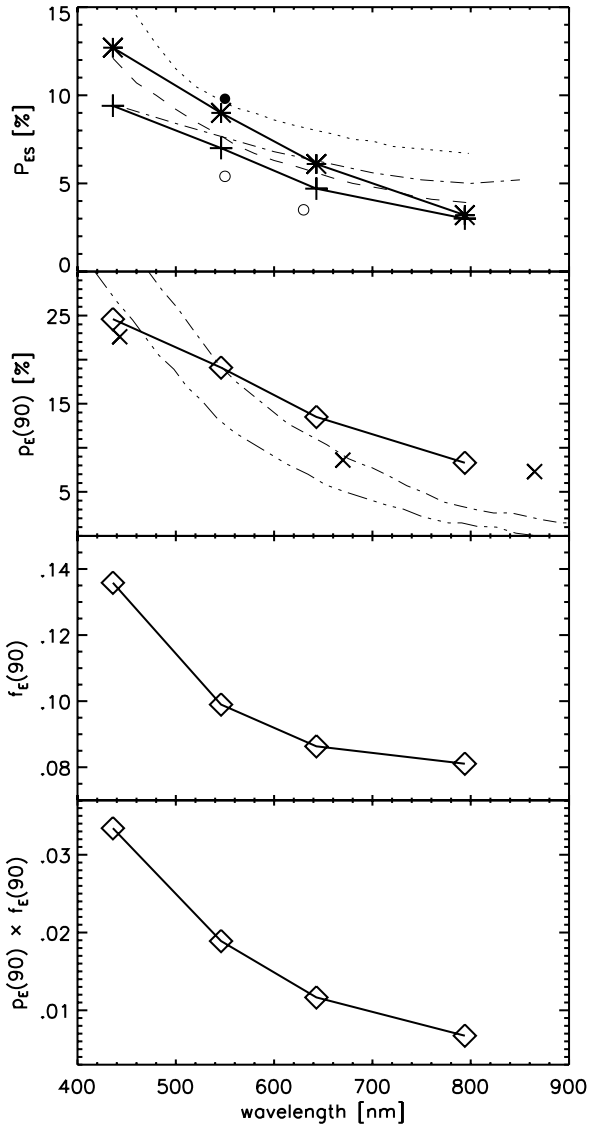

Fig. 13. *Top*: Earthshine polarization results at quadrature for maria (∗) and highlands (+). The thin lines give the Sterzik et al. (2012) spectro-polarimetry for waning (dashed) and waxing (dotted) moon at Earth phases 87° and 102°, respectively, and the Takahashi et al. (2013) spectro-polarimetry (dash-dot) at 96°. The circles are the Dollfus (1957) values q_{max} from Fig. 7 (filled) and two additional observations at Earth phase ≈100° (open). *2nd panel*: Earth polarization p_E from Table 3 (⋄) compared to the POLDER/ADEOS results of Wolstencroft & Breon (2005) (×) and two Stam (2008) models with 40% (dash-dot) and 60% (dash-dot-dot) cloud coverage. *Bottom two panels*: spectral reflectivity of Earth f_E and polarized reflectivity of Earth $p_E \times f_E$.

the mare/highland depolarization difference (or surface albedo difference).

Another spectra-polarimetric observation of the earthshine was published by Takahashi et al. (2013). They also find a rise in the fractional polarization of the earthshine toward the blue but with a much flatter slope. Unfortunately, they do not report whether their results were obtained from maria or highlands either. Therefore, only a qualitative comparison with our data can be made. The observations of Takahashi et al. (2013) are conducted on five consecutive nights and cover phase angles $\alpha = 49°–96°$. In the blue they find that the maximum polarization is reached at $\alpha \approx 90°$. However, for wavelengths >600 nm, the polarization keeps increasing up to and including their last measurement at $\alpha = 96°$. They conclude that the phase with the highest fractional polarization α_{max} is shifted toward larger phase angles, which could be explained by an increasing contribution of the Earth surface reflection. In our data we do not see this shift, but neither can we exclude it because we were not able to derive meaningful data due to the very strong stray light from the moonshine and the weak signal from the earthshine. In this regime our linear extrapolation method of subtracting the background stray light from the earthshine signal introduces a strong systematic overestimate Δ_{syst} of the result (see Sect. 4.2). Takahashi et al. (2013) also use a linear extrapolation method to determine the earthshine polarization, but unfortunately they do not describe their data reduction in detail. Therefore, considering the limitations of our linear extrapolation, it could be possible that the shift of α_{max} reported by Takahashi et al. (2013) is due to the strong stray light at phase angles >90°.

Overall, the spectral dependence of the polarization of Sterzik et al. (2012) and Takahashi et al. (2013) is qualitatively similar to our measurements, but the level and slope of the fractional polarization differ quantitatively. Because Sterzik et al. (2012) and Takahashi et al. (2013) provide no information about the lunar surface albedo for their measuring area and do not assess the stray light effects from the bright moonshine, their results cannot be used for a quantitative test of our results. The spectral slope of Sterzik et al. (2012) is slightly steeper than ours, while the slope of Takahashi et al. (2013) is slightly flatter.

For an assessment of the polarization efficiency for the lunar backscattering we used literature data for polarimetric measurements of lunar samples by Hapke et al. (1993, 1998) and derived a wavelength and surface-albedo dependent polarization efficiency relation $\epsilon(\lambda, a_{603})$, which gives $\epsilon(V, 0.11) = 50.8\%$ for mare in the V band. This value is significantly higher than the 33% derived by Dollfus (1957), which he based on the analysis of volcanic samples from Earth used as a proxy for the lunar maria. Because of this, the Earth polarization derived in this work is much lower than the value given in Dollfus (1957). We are not aware of other studies of the polarization efficiency ϵ for the lunar backscattering. Relying on the determination of ϵ on real lunar soil is certainly an important step in the right direction for a more accurate determination of the polarization of Earth.

Very valuable are the reported Earth polarization values from Wolstencroft & Breon (2005) based on direct polarization measurements with the POLDER instrument on the ADEOS satellite. They derived the fractional polarization for the wavelengths 443 nm (B'), 670 nm (R'), and 865 nm (I') for different surface types and cloud coverage. Weighted mean values representative of an integrated planet Earth observation (55% cloud coverage) of 22.6%, 8.6%, and 7.3% in the B', R', and I' bands are obtained, which are also indicated in the second panel of Fig. 13. The good agreement between our derivation based on the earthshine and the values from Wolstencroft & Breon (2005) confirms our determination of the polarization efficiency. Unfortunately, it is not possible to assess whether the R band point of this study differs significantly from the value of Wolstencroft & Breon (2005) because they give no description of their data and uncertainties.

7.3. Comparison with the models from Stam (2008)

The study of Stam (2008) is unique for modeling the spectral dependence of the fractional polarization of Earth-like planets. In her work she also explored dependencies on a range of physical properties different from Earth's. For our comparison we pick

the model for an inhomogeneous Earth-like planet with 70% of the surface covered by a specular reflecting ocean and 30% by deciduous forest (Lambertian reflector with an albedo for forest), and cloud coverages 40% and 60%. When compared to our Earth polarization determinations (Fig. 13, second panel), these models agree with our measurements at short wavelengths but show a clear deficit in the fractional polarization at long wavelengths in the I band. This is not surprising since the models were not tuned to the case of Earth. In the models, only very thick, liquid water clouds were included, but no thin liquid water clouds and no ice clouds. Karalidi et al. (2012) shows that with more realistic cloud properties for Earth, the degree of polarization can vary strongly depending on the cloud's optical thickness. Our data could now be used to test and to improve model calculations for the Earth polarization.

7.4. Polarization flux contrast for the Earth – Sun system

A key parameter for the polarimetric search and characterization of Earth-like extrasolar planets is the polarization flux $p \times f$ of a planet or the polarization flux contrast C_p as described in Eq. (2). The polarization flux of a highly polarized planet is easier to measure than the fractional polarization p, because the reflected intensity cannot be distinguished easily from the scattered light halo of the central star in high contrast observations. But because stars are essentially unpolarized, it should be possible to detect a differential signal of polarized light from extrasolar planets with high contrast polarimetric imagers as foreseen for the upcoming instrument SPHERE/VLT and planned for future facilities like the E-ELT (e.g. Schmid et al. 2006; Beuzit et al. 2008; Kasper et al. 2010). The polarimetric detection of an Earth-like planet is difficult; nonetheless, it is useful to have accurate values for the expected signal to plan such observations.

The prediction of the polarization flux of an exo-Earth requires besides the fractional polarization $p(\alpha, \lambda)$ determined in this work also the reflected intensity $f(\alpha, \lambda)$. The reflected intensity of Earth can be split into a wavelength dependent geometric albedo term $A_g(\lambda) = f(0°, \lambda)$ and a normalized phase dependence $\Phi(\alpha)/\Phi_0$ where $\Phi_0 = \Phi(\alpha = 0)$ according to

$$f(\alpha, \lambda) = A_g(\lambda) \frac{\Phi(\alpha)}{\Phi_0}.$$

With this approach we neglect the color dependence of the phase curve, which is not known but certainly small when compared to the measuring uncertainties for the spectral albedo $A_g(\lambda)$ and the uncertainties in the fractional polarization $p_E(\lambda, \alpha)$.

The visual geometric albedo of Earth is $A_g(V) = 0.367$ (Cox 2000). With the relative spectral reflectance measured by Arnold et al. (2002), Woolf et al. (2002), and Montañés-Rodriguez et al. (2005), we deduce the geometric albedo for the individual B, V, R, and I filters as given in Table 3.

For the phase dependence $\Phi(\alpha)/\Phi_0$ we use the phase curve determined by Pallé et al. (2003) for the 400−700 nm filter normalized to the B, V, R, and I band geometric albedos derived above. The derived phase curves are given in Fig. 1, and their value for $\Phi(90°)/\Phi_0 = 0.27$ yields the polarized reflectivity for quadrature phase $p_E(90) \times f_E(90)$ for the B, V, R, and I filters as plotted in Fig. 13 and given in Table 3.

The phase curve f_E of Pallé et al. (2003) is based on earthshine measurements at phases between $\alpha = 30°-145°$ extrapolated to $\alpha = 0°-180°$. This broad phase angle coverage is unique and remains, to our knowledge, the only available observation of the phase dependence $\Phi(\alpha)$ of f_E. For future reference we also give in Table 3 the phase integral parameter A_s/A_g, the ratio between spherical and geometric albedo, derived from the Pallé et al. (2003) data.

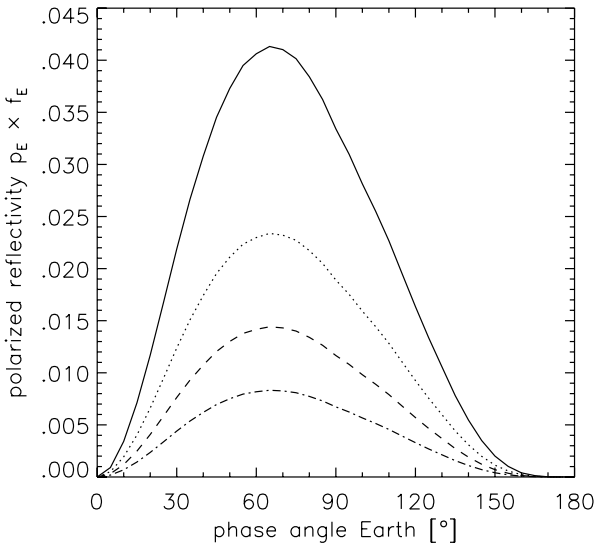

Fig. 14. Polarized reflectivity phase curve $p_E(\alpha) \times f_E(\alpha)$ for Earth in the B (solid), V (dotted), R (dashed), and I band (dash-dot).

Table 3. Geometric albedo A_g, phase integral A_s/A_g, and quadrature results for the planet Earth.

	B	V	R	I
A_g	0.504	0.367[1]	0.320	0.301
A_s/A_g	0.86	0.86	0.86	0.86
values for $\alpha = 90°$				
p_E [%]	24.6	19.1	13.5	8.3
Δp_E [%]	±1.2	±1.3	±0.9	±1.4
f_E	0.136	0.099	0.086	0.081
$p_E \times f_E$ [10^{-3}]	33.41	18.90	11.66	6.73
C_p [10^{-11}]	6.07	3.44	2.12	1.22

Notes. Given are the fractional polarization p_E, the Earth reflectivity f_E,the polarized reflectivity $p_E \times f_E$, and the polarization contrast $C_p = p_E \times f_E \times (R_E/d_{S-E})^2$ for an Earth-Sun system. The systematic offset uncertainty Δp_E is due to the uncertainty of the depolarization and albedo of the lunar surface.

References. [(1)] Cox (2000).

The spectral dependence of the polarization flux $p_E(\lambda, 90°) \times f_E(\lambda, 90°)$ of Earth decreases steeply toward longer wavelengths, because both the fractional polarization p_E and the reflectivity f_E are higher for the blue than for the red. The $p_E \times f_E$ signal in the B band is about a factor five times stronger than in the I band.

The polarization contrast $C_p(\lambda, 90°)$ according to Eq. (2) is determined from $p_E \times f_E$ and using R_E^2/AU^2. This yields values at the level of a few times 10^{-11} only (Table 3). One should note that an Earth-like planet in the habitable zone of an ≈M4V star with $L = 0.02\ L_\odot$ is at a much smaller separation of 0.14 AU. In this case the expected polarization contrast is about a factor of 50 higher and within reach for a high contrast imaging polarimeter at an ELT (Kasper et al. 2010).

The B, V, R, and I phase curves for the polarized reflectivity $p_E \times f_E$ are plotted in Fig. 14. The maximum signal occurs near $\alpha \approx 65°$, which is thus the best phase for a detection.

8. Summary and discussion

This work presented measurements of the earthshine polarization in the B, V, R, and I bands. The data were acquired with a specially designed, wide-field imaging polarimeter using a focal plane mask to suppress the light from the bright lunar crescent. Thanks to this measuring method we could accurately correct for contributions from the (twilight) sky and the scattered light from the bright lunar crescent and derive values with well-understood uncertainties. We derived phase curves for the fractional polarization for the earthshine reflected from maria and highlands for the different filter bands. The phase curves can be fit with the sine-square function $q_{\max} \sin^2(\alpha)$. The amplitude $q_{\max}$ decreases strongly with wavelength from about 13% in the B band to about 3% in the I band (see Table 2). The fractional polarization of the earthshine is about a factor 1.3 higher for the dark mare region when compared to the bright highland. Our phase curve for the mare region in the V band is in close agreement with the historic visual polarization phase curve from Dollfus (1957).

We studied the depolarization introduced by backscattering at the lunar surface based on published polarimetric measurements of lunar samples (Hapke et al. 1993, 1998). We derived a two-dimensional fit function for the polarization efficiency $\epsilon(\lambda, a_{603})$ of the backscattering, which depends on wavelength and surface albedo. Earthshine measurements plus ϵ correction yield as the main result of this paper the fractional polarization of the reflected light from the planet Earth as a function of phase in four bands. The polarization of Earth in quadrature phase is as high as 25% in the B band and decreases steadily with wavelength to 8% in the I band (see Table 3). Similar values have been reported from direct satellite measurements of the Earth polarization (Wolstencroft & Breon 2005).

This work provides the most comprehensive measurements of the polarization of the integrated light of the planet Earth up to now. The determined values can be used as benchmark values for tests of polarization models and for predictions for future polarimetric observations of Earth-like extrasolar planets. In particular, we accurately described our measurements and assessed the uncertainties. In addition we applied a polarization efficiency ϵ correction. For the first time, it is based on lunar soil measurements and is significantly different from previously used volcanic rock measurements.

Similar to our data of Earth, the models of Stam (2008) for horizontally inhomogeneous Earth-like planets with thick liquid water cloud coverage show also a decrease in fractional polarization with wavelength but with a significantly steeper slope. This may indicate that other scattering components, for example aerosols, thin liquid water clouds, and ice clouds contribute significantly to the Earth polarization in the I band (see Karalidi et al. 2012).

Are our polarization values for the planet Earth representative or should we expect large temporal variations? Our data were taken during two observing runs each lasting a few days. Two data sets are from similar phase angles, 73.0° and 75.5°, but they were taken seven months apart. The measured fractional polarization differs by about $\Delta q/q \approx 0.1$. Also the deviation of the data points from the fit $q_{\rm fit} = q_{\max} \sin^2 \alpha$ is at the same level $(|q - q_{\rm fit}|)/q \approx 0.1$. This scatter is at the level of our calibration errors. Therefore, variation in the intrinsic polarization signal of Earth on the 10% level could be present in our data without being recognized. Our measurements certainly show no changes at the $\Delta q/q \approx 0.3$ level as suggested by Sterzik et al. (2012). Variations in the fractional polarization are of interest because they could be used as a diagnostic tool for investigations of surface structures or temporal changes in the cloud coverage of extrasolar planets.

Because our study includes a detailed assessment of the uncertainties for each step in our determination, we can now discuss how the Earth polarization measurement could be improved. Polarization variability studies could be carried out with enhanced sensitivity by selecting observing periods and filters with strong earthshine polarization signals in order to minimize statistical noise and systematic effects in the data extraction. Observations in the B and V filter, and for phase angles in the range from $\alpha = 40°$ to 100°, would be ideal for such studies. Measurements taken for several consecutive nights would allow a sensitive search for day-to-day variations at a level of $\Delta q/q \approx 0.03$ owing to variable cloud coverage. Also multiple-epoch data could be collected for an investigation of long-term and seasonal polarization changes.

The determination of a more accurate wavelength dependence of the earthshine polarization could be established with long integrations for phase angles between 50°–80° when the earthshine polarization signal is strong, the level of scattered light from the moonshine still low, and the time for observations after twilight long enough for observations in multiple filters.

More accurate phase curves require careful analysis of the data from different phases because the earthshine observing conditions and the associated measuring and calibration procedures change strongly with lunar phase. If these problems can be solved, then one could accurately determine the peak in the fractional polarization curve near $\alpha = 90°$ as function of wavelength and investigate the presence of a rainbow feature in the polarization data around $\alpha = 40°$ (see Stam 2008).

A more accurate absolute value for the polarization of the planet Earth first requires more data to average out intrinsic variations. Equally important is a more accurate determination of the surface albedo for the measuring region and the associated polarization efficiency $\epsilon(\lambda, a_\lambda)$ for the correction of the lunar backscattering.

The imaging polarimetry of the earthshine presented in this study and the spectro-polarimetric results from Sterzik et al. (2012) and Takahashi et al. (2013) demonstrate that investigating the Earth polarization via earthshine measurements is very useful and attractive. Detailed and versatile investigations are possible with existing polarimetric instruments as used by Sterzik et al. (2012) and Takahashi et al. (2013) or with small, specific experiments as demonstrated in this work. The obtained results can be compared with model calculations like those described in Stam (2008) and teach us about the light-scattering processes of planets. Because we know our Earth so well, we can also investigate subtle effects, which are potentially important in other planets. Building up our knowledge of scattering polarization from Earth could therefore become important for the future polarimetric investigation of extrasolar planets.

Acknowledgements. Part of this work was supported by the FINES research fund by a grant through the Swiss National Science Foundation (SNF).

References

Arnold, L., Gillet, S., Lardière, O., Riaud, P., & Schneider, J. 2002, A&A, 392, 231
Bailey, J. 2007, Astrobiology, 7, 320
Bessell, M., & Murphy, S. 2012, PASP, 124, 140
Beuzit, J.-L., Feldt, M., Dohlen, K., et al. 2008, in SPIE Conf. Ser., 7014
Bhatt, H. C., & Manoj, P. 2000, A&A, 362, 978
Cox, A. N. 2000, Allen's astrophysical quantities (New York: AIP Press: Springer)
Coyne, G. V., & Pellicori, S. F. 1970, AJ, 75, 54

Dollfus, A. 1957, Supplements aux Annales d'Astrophysique, 4, 3
Dollfus, A., & Bowell, E. 1971, A&A, 10, 29
Dumusque, X., Pepe, F., Lovis, C., et al. 2012, Nature, 491, 207
Gehrels, T., Coffeen, T., & Owings, D. 1964, AJ, 69, 826
Hamdani, S., Arnold, L., Foellmi, C., et al. 2006, A&A, 460, 617
Hapke, B. W., Nelson, R. M., & Smythe, W. D. 1993, Science, 260, 509
Hapke, B., Nelson, R., & Smythe, W. 1998, Icarus, 133, 89
Howard, A. W., Marcy, G. W., Bryson, S. T., et al. 2012, ApJS, 201, 15
Hsu, J.-C., & Breger, M. 1982, ApJ, 262, 732
Karalidi, T., Stam, D. M., & Hovenier, J. W. 2011, A&A, 530, A69
Karalidi, T., Stam, D. M., & Hovenier, J. W. 2012, A&A, 548, A90
Kasper, M., Beuzit, J.-L., Verinaud, C., et al. 2010, in SPIE Conf. Ser., 7735
Kieffer, H. H., & Stone, T. C. 2005, AJ, 129, 2887
Lyot, B. 1929, Ann. Obs. Meudon, 8, 1
Macintosh, B. A., Anthony, A., Atwood, J., et al. 2012, in SPIE Conf. Ser., 8446
Mayor, M., Marmier, M., Lovis, C., et al. 2011, A&A, submitted [arXiv:1109.2497]
Montañés-Rodriguez, P., Pallé, E., Goode, P. R., Hickey, J., & Koonin, S. E. 2005, ApJ, 629, 1175
Montañés-Rodríguez, P., Pallé, E., & Goode, P. R. 2007, AJ, 134, 1145
Noble, S. K., Pieters, C. M., Taylor, L. A., et al. 2001, Meteorit. Planet. Sci., 36, 31
Pallé, E., Goode, P. R., Yurchyshyn, V., et al. 2003, J. Geophys. Res. (Atmospheres), 108, 4710
Qiu, J., Goode, P. R., Pallé, E., et al. 2003, J. Geophys. Res. (Atmospheres), 108, 4709
Schmid, H. M., Beuzit, J.-L., Feldt, M., et al. 2006, in Direct Imaging of Exoplanets: Science & Techniques, eds. C. Aime, & F. Vakili, IAU Colloq., 200, 165
Shkuratov, Y., Kaydash, V., Korokhin, V., et al. 2011, Planet. Space Sci., 59, 1326
Stam, D. M. 2008, A&A, 482, 989
Sterzik, M. F., Bagnulo, S., & Palle, E. 2012, Nature, 483, 64
Takahashi, J., Itoh, Y., Akitaya, H., et al. 2013, PASJ, 65, 38
Tinbergen, J. 1996, Astronomical Polarimetry (Cambridge, UK: Cambridge University Press)
Turnshek, D. A., Bohlin, R. C., Williamson, II, R. L., et al. 1990, AJ, 99, 1243
Velikodsky, Y. I., Opanasenko, N. V., Akimov, L. A., et al. 2011, Icarus, 214, 30
Williams, D. M., & Gaidos, E. 2008, Icarus, 195, 927
Wolstencroft, R. D., & Breon, F.-M. 2005, in Astronomical Polarimetry: Current Status and Future Directions, eds. A. Adamson, C. Aspin, C. Davis, & T. Fujiyoshi, ASP Conf. Ser., 343, 211
Woolf, N. J., Smith, P. S., Traub, W. A., & Jucks, K. W. 2002, ApJ, 574, 430